Communication

Nan Yang*, Yong Deng*, Jinlun Huang, and Xiaodong Niu*

Structural material with designed thermal twist for a simple actuation

https://doi.org/10.1515/ntrev-2022-0026
received October 17, 2021; accepted December 11, 2021

Abstract: Materials with desired thermal deformation are very important for various engineering applications. Here, a material with the combination of chiral structure and TiNi shape memory alloy (SMA) sheets that performs a twist during heating is proposed. The thermo-mechanical properties of these materials are experimentally investigated. Inspired by this, a car-like material performing translational and rotational motion is designed, which illustrates the potential applications for the next-generation soft robotic devices. Based on this method, one can design remotely manipulated artificial muscles, nanorobots, revolute pairs, and thermal sensors or actuators in a noncontact fashion.

Keywords: heat-driven actuators, kinematics properties, coupled thermo-mechanical properties, chiral structures, shape memory alloys

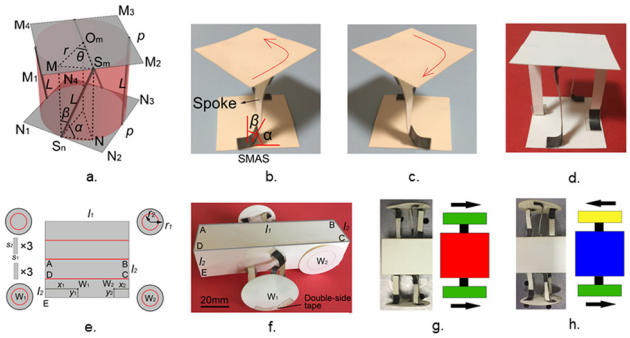

Graphical abstract: (a) Geometrical model, (b) anti-clockwise, (c) clockwise, (d) chiral structure with SMA, (e) 2D car model, (f) 3D car model, (g) two wheels in identical direction, (h) two wheels in opposite direction.

1 Introduction

Mechanical metamaterials with artificial architectures show interesting properties with ultralight masses [1], cloaking functions [2,3], reprogrammable mechanical properties [4], heat flux manipulation [5], and tunable sonic frequency [6]. Further, mechanical metamaterials with auxetic properties have been attractive in the fields of physics and engineering due to their unique responses, such as negative Poisson's ratio, negative stiffness, negative effective mass/modulus, indention resistance, energy dissipation, and acoustic absorption properties [7–13]. They can be applied in the blast resistance materials [14,15], flexible electronics [16], morphing airfoils [17], bioimplants [18,19], nanorobots [20,21], and sensors and actuators [22].

Auxetic metamaterials mainly have three categories: reentrant materials, rigid square rotation materials, and chiral structures [23]. In chiral structures, chiral elasticity theory can describe the coupling among local rotation, bending, and bulk deformation [24–27]. Based on this theory, the deformation mechanism of tension–torsion coupling [29], dilatation–rotation coupling, and shear–rotation coupling [27,28] of chiral structures is well investigated. Our heat-driven actuators are motivated by the chiral structures that have a tension–torsion coupling effect. For example, an elastic bar designed with a man-made architecture performed a twist during compression, which was mainly caused by the circumferential freedoms of a unit cell [29]. Similarly, a tetrachiral cylindrical shell based on the natural plant architecture exhibited a reversible bidirectional twisting deformation in the axial compression and tension processes [30]. Then, three-dimensional (3D) architectures with the coupling effect of shear-compression also exhibited a twist behavior under uniaxial loading [31], and the tension–torsion

* **Corresponding author: Nan Yang,** Intelligent Manufacturing Key Laboratory of Ministry of Education, Shantou University, Shantou 515063, China, e-mail: nyang@stu.edu.cn
* **Corresponding author: Yong Deng,** Intelligent Manufacturing Key Laboratory of Ministry of Education, Shantou University, Shantou 515063, China; Digital Technology Research and Application Center, Shantou Polytechnic, Shantou 515078, China, e-mail: dengyong@stu.edu.cn
* **Corresponding author: Xiaodong Niu,** Intelligent Manufacturing Key Laboratory of Ministry of Education, Shantou University, Shantou 515063, China, e-mail: xdniu@stu.edu.cn
Jinlun Huang: Intelligent Manufacturing Key Laboratory of Ministry of Education, Shantou University, Shantou 515063, China

coupling effect was found based on a 3D metamaterial with connecting neighbor chiral honeycomb layers [32].

The aforementioned literature has been focused on the twist behavior caused by uniaxial force, but here, we use the chiral structure in a different way: harvesting twist with heating. The chiral structures are actuated by shape memory alloy (SMA) sheets, which can be deformed when cold but return to their predeformed shapes when heated. The deformation recovery effect and hyperelastic property of SMAs are associated with a diffusionless martensitic transformation [33,34]. Hence, they can be trained to remember their shape at both high temperature phase (austenite phase) and low temperature phase (martensite phase), which was used in this research as a two-way memory effect [34,35]. The combination effects of SMA with purposely engineered topologies have been paid more attention. Grummon *et al.* [36,37] created a regular cellular material by joining thin-walled superelastic SMA tubes *via* electrical resistance welding and explored the influence of constitutive behavior on the effective mechanical properties. Hassan *et al.* [37,38] manufactured truss by assembling cells of chiral honeycomb topology and SMA ribbons, which have a large rotational folding rate to use in new types of deployable antenna reflectors. Moreover, SMAs have been used as torsional actuators by converting the linear actuation motion or directly rotational motion in many practical fields, such as biomedical applications, aerospace applications, and automotive applications. The linear actuation motion caused by the contractile behavior of SMA wires, springs, or thin films is used to generate rotation, and the direct rotational motion with slender SMA torque tubes and rods twisted around the long axis is used to achieve direct rotation [34]. These methods use the SMA component to form rotational actuators. In this research, we combine SMA sheets and chiral structures (Figure 1a) to realize twistable actuators, as the twist comes from the coupling between SMA sheets and chiral structures, which opens a new avenue for torsional SMA-based actuators. Compared to the fiber-based actuators that can only directly produce pulling force [39–41] and the hydraulically amplified self-healing electrostatic actuators that can only directly generate propulsive force [42], our chiral structures actuated by SMA sheets can yield both pulling force and propulsive force. Compared to the electrohydraulic transducer-based actuators [43], our design scheme needs simpler devices and can produce a larger strain. Here, the geometries, kinematics, and coupled thermo-mechanical properties of these motors on a macroscale are experimentally investigated. However, the proposed method is also appropriate on a nanoscale, which can be used in nanorobots and actuators.

2 Experimental

2.1 Geometry design of a motor

Figure 1a shows that the motor consists of the upper square $M_1M_2M_3M_4$ (with center point O_m), lower square $N_1N_2N_3N_4$ (length $\overline{M_1M_2} = \overline{N_1N_2} = p = 40$ mm), and four spokes (*e.g.*, S_mS_n with length L, where S_m and S_n are middle points of sides M_1M_2 and N_1N_2, respectively, and the distance between points S_m and O_m is r. Additionally, see the photos in Figure 2b–d for the way that real spokes connect with the upper and lower squares using SMA sheets). Angle $\alpha = \angle S_mS_nN$ denotes the angle between one spoke and the upper/lower square $\left(\beta = \frac{\pi}{2} - \alpha\right)$. θ denotes the angle that the upper square is twisted relative to the lower square. There are four geometrical parameters determining the whole structure with the relation $2r \sin\left(\frac{\theta}{2}\right) = L \cos(\alpha)$, which can basically predict the change of angle θ (Figure 2a, inset). The key idea is using SMA sheets to control the change in angle α and obtain a twist (change in angle θ). Here, $L = 40$ mm, and $r = 20$ mm.

2.2 Properties of TiNi SMA sheets

In this study, two-way memory TiNi SMA sheets (Zhilian Memory Alloy Co., Ltd., Huizhou, China) with the initial angle $\alpha \approx 90°$ were used. During heating, the SMA sheet straightened with the decrease in angle α. When the heater was turned off, the SMA sheet slowly returned to its initial shape as it was cooled to room temperature. The properties of TiNi SMAs are shown in Table 1, which are consistent with the earlier literature [33]. Here, the SMA sheet sizes of all samples are as follows: 6 mm (width) × 14 mm (length) × 0.4 mm (thickness).

2.3 Fabrication of the motors

For fabricating the motors, a U.S. Strathmore 500 Series 3-ply Bristol card stock (U.S. Strathmore) cut by laser forming the structure and TiNi SMA sheets controlling the angle α were used. The photographs in Figure 2b show how a spoke and the upper/lower square are connected by a TiNi SMA sheet. For each spoke, two SMA sheets were used to connect the upper and lower squares. Therefore, four SMA sheets were needed for the motor with two spokes, and six SMA sheets are needed for that with three spokes, and so on.

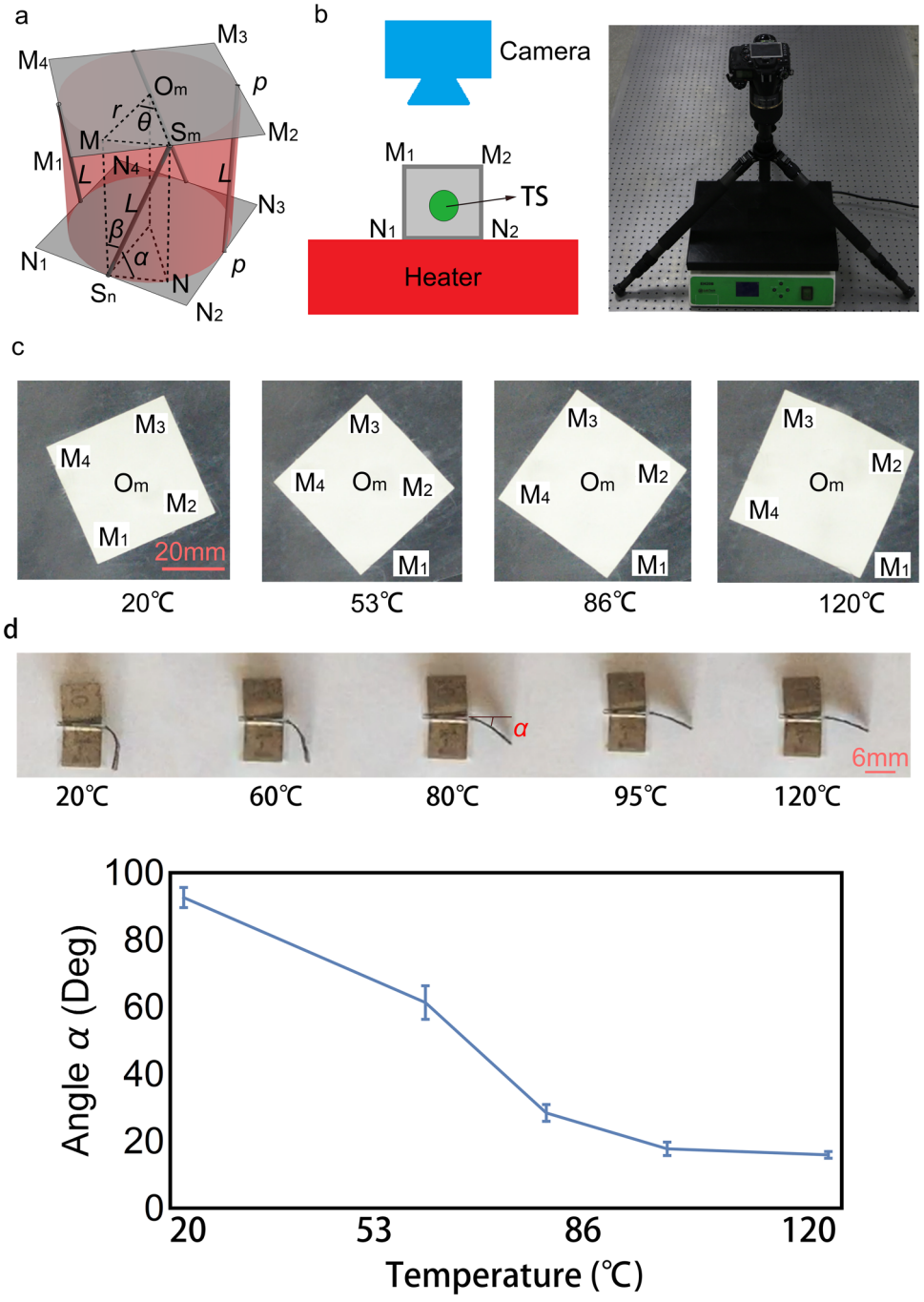

Figure 1: (a) Geometrical model of the motor with four spokes. (b) Experimental scheme and photograph of the experimental setup. (c) Photographs of the motor's upper surface captured at four instantaneous moments. (d) Photographs of a TiNi SMA sheet with one side fixed during heating. Half of the TiNi SMA sheet is fixed between two "V"-shaped steel sheets, and another half is free. The plot shows angle α as a function of temperature. The error bars are based on four SMA sheets. Each SMA sheet was measured three times.

2.4 Motion capture

To measure the twist angle θ of the motor as a function of temperature, the experimental setup, as shown in Figure 1b (scheme and photograph), was built. A platform controlling the temperature from 20 to 120°C was used to heat the motor, which meant that the heater could heat the SMA sheets in a noncontact way. A temperature sensor was placed in the motor to obtain the temperature near the SMA sheets. A camera from the top was used to record the motion of the upper square $M_1M_2M_3M_4$, which can be seen in Figure 1c at each temperature.

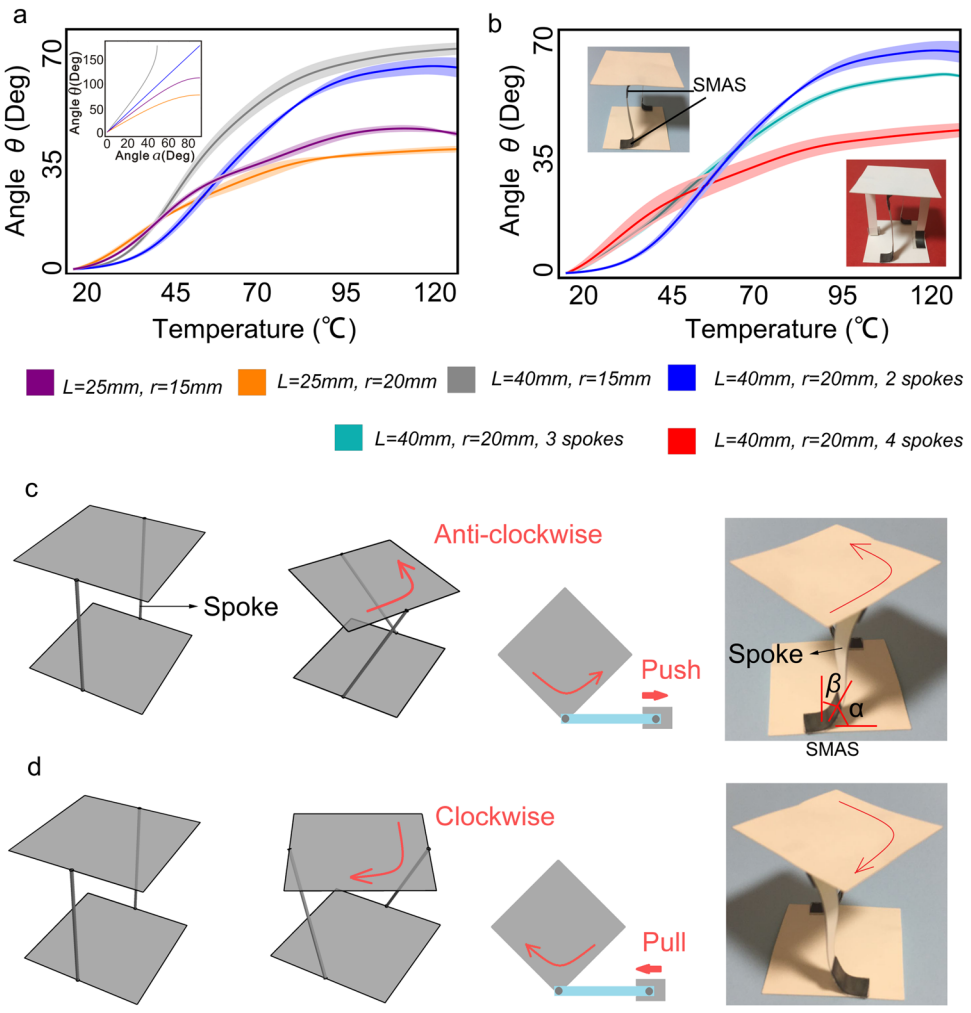

Figure 2: (a) θ – temperature relationship with different geometrical parameter combinations, inset: θ – α relationship with different geometrical parameter combinations. (b) θ – temperature relationship with different number of spokes. The color rule of the curves is shown below the plots (with two spokes: purple: L = 25 mm and r = 15 mm, orange: L = 25 mm and r = 20 mm, gray: L = 40 mm and r = 15 mm, and blue: L = 40 mm and r = 20 mm; with three spokes: cyan: L = 40 mm and r = 20 mm; and with four spokes: red: L = 40 mm and r = 20 mm). For each experimental result with an individual color, the central curve shows the average of three measurements, and the region contains measurement errors. (c) The motor with anticlockwise twist producing propulsive force. (d) The motor with clockwise twist producing pulling force.

Table 1: The properties of TiNi SMA

Property of TiNi alloy	Units	Martensite	Austenite
Mean density	g/cm^3	6.45	
Poisson's ratio	—	0.33	
Ultimate tensile strength	MPa	25–40	60–83
Young's modulus	GPa	70–140	195–690
Yield strength	Mpa	70–140	195–690
Thermal conductivity	W/(m K)	8.6	18
Coefficient of thermal expansion	K^{-1}	6.6	11

To focus on the upper square $M_1M_2M_3M_4$, the spokes and lower square $N_1N_2N_3N_4$ were made using black card stock, which were invisible in the black ground of the heater surface. Thus, only the upper square $M_1M_2M_3M_4$ was in white color and could be clearly recognized by the camera. First, we calibrated the overall system and obtained the ratio of real size to pixel (0.073 mm per pixel). Corner points M_1, M_2, M_3, M_4 were recognized, and their 2D coordinates that changed over heating time were obtained. Based on this, the coordinate of center point O_m can be defined as $(\sum_{i=1}^{4} x_i/4, \sum_{i=1}^{4} y_i/4)$, where

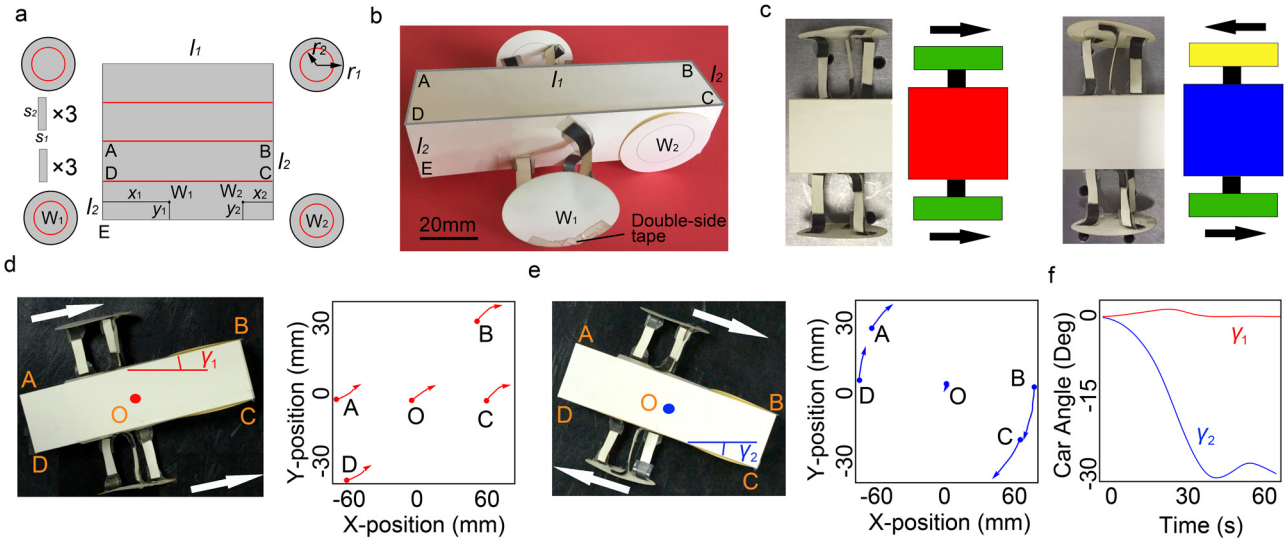

Figure 3: (a) 2D design scheme of the car. (b) Photograph of the car with heat-driven motors. (c) Two action wheels on the two sides of the car twisting (left) in identical direction and (right) in opposite direction. (d) Translational motion of the car (photograph and red trajectories of the five points on the car surface). (e) Rotational motion of the car (photograph and blue trajectories). (f) Measurements of the car body angles regarding the (red) translational motion and (blue) rotational motion.

(x_i, y_i) denotes the coordinate of M_i. The twist angle, θ, can be evaluated as $\theta = (\theta_{1,3} + \theta_{2,4})/2$, where $\theta_{1,3} = \cos^{-1}\left(\frac{\boldsymbol{M}_{13}|_t \cdot \boldsymbol{M}_{13}|_{t_0}}{|\boldsymbol{M}_{13}|_t \cdot |\boldsymbol{M}_{13}|_{t_0}}\right)$ and $\theta_{2,4} = \cos^{-1}\left(\frac{\boldsymbol{M}_{24}|_t \cdot \boldsymbol{M}_{24}|_{t_0}}{|\boldsymbol{M}_{24}|_t \cdot |\boldsymbol{M}_{24}|_{t_0}}\right)$.

$\boldsymbol{M}_{ij}|_{t_0}$ and $\boldsymbol{M}_{ij}|_t$ denote vector $\boldsymbol{M}_{ij}$ at initial moment t_0 and instantaneous moment t, respectively. $|\boldsymbol{M}_{ij}|_{t_0}$ and $|\boldsymbol{M}_{ij}|_t$ denote the lengths of vector $\boldsymbol{M}_{ij}$ at initial moment t_0 and instantaneous moment t, respectively, where $\boldsymbol{M}_{ij} = M_j - M_i$.

3 Results and discussion

3.1 Investigation of one SMA sheet

An SMA sheet with one side fixed was heated, and another side was free. At 20°C, the angle α of the SMA sheet was about 90° (see photograph in Figure 1d). During heating, the SMA sheet straightened itself, thus α decreased, as shown in the plot of Figure 1d. The angle α decreased rapidly as the temperature increased from 20 to 95°C and remained constant at 95–120°C; the minimum value of α was about 16°, which reveals that the SMA sheet realized the deformation within the temperature range of 20–120°C. Assembling the SMA sheets to a chiral structure (Figure 1a) to control the angle α caused a twist angle θ of the motor; thus, this mechanism enabled the chiral structure to act as a motor.

3.2 Kinematic properties of motors

Experimentally, the twist angle θ, as a function of temperature with different geometrical parameters of L and r, was measured. In Figure 2a, angle θ quickly increased before 95°C and then basically remained constant. A large value of length L resulted in a large change in θ (see the orange data *vs* blue data, and purple data *vs* gray data). Additionally, a small value of r also resulted in a large change in θ (see the orange data *vs* purple data, and blue data *vs* gray data). In Figure 2b, we experimentally found that the value of θ of the motor with two spokes was larger than that with three spokes and four spokes, by fixing the other geometrical parameters (see the blue data *vs* cyan data *vs* red data), which indicates that more constraints may hamper the twist behavior of the motor. Interestingly, if we change the direction of the SMA sheets connecting spokes with squares, the twist can be both anticlockwise (Figure 2c model and photo) and clockwise (Figure 2d model and photo), which can yield both propulsive force and pulling force (see the third column of Figure 2c and d).

3.3 Kinematic properties of a car assembled with such motors

Interestingly, such actuators can be used to drive a car. In Figure 3a and b, the size of the car body was $l_1 \times l_2 \times l_2$,

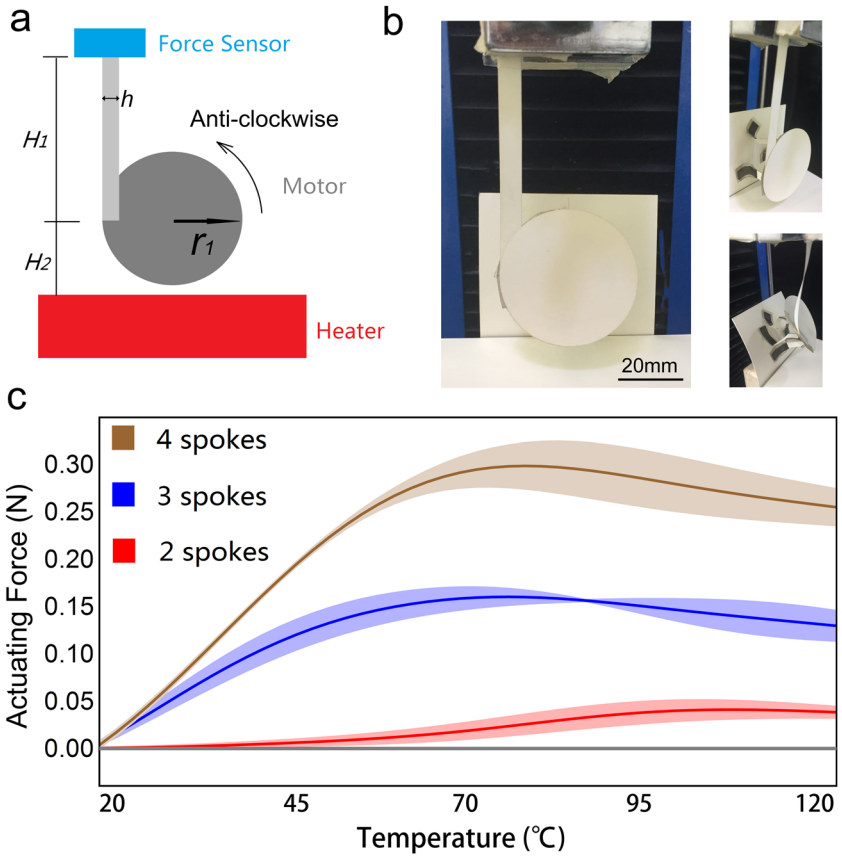

Figure 4: (a) Experimental scheme to measure the actuating forces of the heat-driven motors, where $H_1 = 63$ mm, $H_2 = 22$ mm, $h = 6$ mm, and $r_1 = 20$ mm. (b) Experimental photographs. (c) Actuating force as a function of temperature with two (red), three (blue), and four (brown) spokes. The size of each spoke is 6 mm × 25 mm. For each experimental result with an individual color, the central curve shows the average of three measurements, and the region contains the measured errors.

where $\overline{AB} = l_1$ and $\overline{BC} = \overline{DE} = l_2$ ($l_1 = 4l_2 = 120$ mm). Each wheel with radius $r_1 = 20$ mm was fixed on the car body based on the center points, such as W_1 (action wheel) and W_2 (driven wheel). The wheels were obtained by changing the squares (*e.g.*, $M_1M_2M_3M_4$ in Figure 1a) to disks. There were two action wheels and two driven wheels on the car body. Each action wheel was connected to the car body with three spokes (with size $s_1 \times s_2 = 6$ mm × 25 mm) and six SMA sheets, and the SMA sheets were evenly arranged along the red circles with radius $r_2 = 12.5$ mm as shown in Figure 3a and b. The driven wheels were directly glued on the car body. The assembling location of action wheel W_1 was $(x_1, y_1) = (50$ mm, 10 mm) based on center W_1, and that of driven wheel W_2 was $(x_2, y_2) = (20$ mm, 10 mm) based on center W_2 (Figure 3a). To enhance the friction between the action wheels and the ground, double-side tapes were used on the edge of action wheels as shown in Figure 3b.

The action wheels on the two sides of the car body can be designed to twist in an identical direction (Figure 3c left) or in opposite directions (Figure 3c right). In Figure 3c, the assembling fashions between the wheels, SMA sheets, and spokes are shown in the photographs, and the arrows indicate the motion directions of the top edges of the action wheels. Figure 3d and e show the walking experiments of the car actuated by the heat-driven motors on the heater from 20 to 120°C recorded using a camera. In Figure 3d, the action wheels on the two sides of the car twist in the same direction (see the white arrows), thus the car exhibited a translational motion (see the red trajectories of the corner points A, B, C, and D and the central point O on the top surface of the car in Figure 3d right, where dots denote starting points and arrows denote terminal points. The measurement method was similar to that in Section 2). This is also demonstrated in Figure 3f with the car body angle $\gamma_1 \approx 0$ (red curve), which is defined as the angle between line AB and its initial direction (Figure 3d left). When the action wheels on the two sides of the car twisted in opposite directions (see the white arrows in Figure 3e left), the car presented a clockwise rotation (see the blue trajectories

in Figure 3e right and the blue curve with $\gamma_2 < 0$ in Figure 3f).

The flaw of this design is that the car can only trigger a stroke, and how to design heat-driven actuators with continuous twist is still an open question.

3.4 Coupled thermo-mechanical properties

Here, an experiment to obtain the actuating force of the heat-driven motors is designed. As shown in Figure 4a, the motor was connected with the force sensor by a thick paper strip and fixed between the force sensor and the heater, where $H_1 = 63$ mm, $H_2 = 22$ mm, $h = 6$ mm, and $r_1 = 20$ mm. Figure 4b shows the photographs of the setup in two views. When heating, the motor twisted anticlockwise (see the arrow in Figure 4a) and pulled the strip, and then pulled the force sensor to obtain the actuating force data. Figure 4c shows the actuating forces of the motors with two, three, and four spokes from 20 to 120°C. As expected, we found that the motor with more spokes yielded a larger actuating force (brown curves). This indicates that increasing the number of spokes is a good way to enlarge the actuating force of the motor. As the paper strip does not allow extension, the paper disk, strip, and spokes all deformed after they were heated, as shown in the lower right photo in Figure 4b, which led to the reductions in force responses after the peak values (brown and blue curves in Figure 4c).

In the future, a finite element model is needed to predict the interaction between the twisting structures and SMA sheets with heating (such as the deformations of spokes and wheels). Furthermore, the load performance of an SMA sheet, the maximum strokes, force and response speed, and efficiency of the motor structure should be investigated. As SMA can be trained to achieve desired deformation within given temperature range [33], SMA sheets used in this paper that transform in narrower temperature range, such as 20–40°C, need to be further improved and studied for convenient application and low energetic cost. Meanwhile, for the perspective of SMA performance development, it is important to understand the microstructural evolution related to the deformation behavior of SMA [44]. The effect of different stages of deformation on the microstructure evolution of SMA has been reported in the available literature [45], which showed that the deformation twinning and stacking fault ribbons were the main deformation mechanisms. Therefore, the effect of microstructure on deformation correlating with the behavior of the proposed actuator needs to be further investigated. Moreover, the design of heat-driven actuator with continuous twist needs to be further considered.

4 Conclusions

Here, the heat-driven actuators made by twisting structures and TiNi SMA sheets are designed. The kinematic properties of the actuators with different geometrical parameters and number of spokes were experimentally studied. Based on such motors, we designed a car and then demonstrated its translational and rotational motion driven by heating. To investigate the coupled thermo-mechanical properties, we measured the actuating force of the motor with different number of spokes. In given thermal conditions, the proposed actuators can provide desired twist and torque in a noncontact way, which can be potentially used as remotely controlled revolute pairs in nanorobots, artificial muscles, bioimplants, and thermal sensors.

Funding information: The authors thank the National Natural Science Foundation of China (11872046), Natural Science Foundation of Guangdong Province (2021A1515010318), Tianjin Natural Science Foundation (18JCZDJC10030), Natural Science Foundation in Shantou University (NTF19012), Key Project of Guangdong Provincial Department of Education (2021ZDZX2007), Special Foundation of science and technology of Guangdong Province (2019ST007), and Cross-Disciplinary Research Funding (2020LKSFG01D).

Author contributions: N.Y. designed the research. N.Y. and Y.D. performed the experiments. N.Y. wrote the original draft of the article. N.Y., Y.D., J.H., and X.N. reviewed and edited the manuscript. All authors have accepted responsibility for the entire content of this manuscript and approved its submission.

Conflict of interest: The authors state no conflict of interest.

Data availability statement: The data and materials of this study are available from the corresponding author upon reasonable request.

References

[1] Schaedler TA, Jacobsen AJ, Torrents A, Sorensen AE, Lian J, Greer JR, et al. Ultralight metallic microlattices. Science. 2011;334(6058):962–5.

[2] Pendry JB, Schurig D, Smith DR. Controlling electromagnetic fields. Science. 2006;312(5781):1780–2.
[3] Bückmann T, Kadic M, Schittny R, Wegener M. Mechanical cloak design by direct lattice transformation. Proc Natl Acad Sci USA. 2015;112(16):4930–4.
[4] Florijn B, Coulais C, van Hecke M. Programmable mechanical metamaterials. Phys Rev Lett. 2014;113(17):175503.
[5] Narayana S, Sato Y. Heat flux manipulation with engineered thermal materials. Phys Rev Lett. 2012;108(21):214303.
[6] Liu Z, Zhang X, Mao Y, Zhu YY, Yang Z, Chan CT, et al. Locally resonant sonic materials. Science. 2000;289(5485):1734–6.
[7] Yang W, Li ZM, Shi W, Xie BH, Yang MB. Review on auxetic materials. Int J Mech Sci. 2004;39:3269–79.
[8] Mir M, Ali MN, Sami J, Ansari U. Review of mechanics and applications of auxetic structures. Adv Mater Sci Eng. 2014;2014:1–17.
[9] Zhang Y, Zhang F, Yan Z, Ma Q, Li X, Huang Y, et al. Printing, folding and assembly methods for forming 3D mesostructures in advanced materials. Nat Rev Mater. 2017;2:17019.
[10] Carneiro VH, Meireles J, Puga H. Auxetic materials-a review. Mater Sci-Pol. 2013;31:561–71.
[11] Grima JN, Manicaro E, Attard D. Auxetic behaviour from connected different-sized squares and rectangles. Proc R Soc A Math Phys Eng Sci. 2010;467(2126):439–58.
[12] Cveticanin L, Zukovic M. On the elastic metamaterial with negative effective mass. J Sound Vib. 2018;436:295–309.
[13] Li Z, Wang C, Wang X. Modelling of elastic metamaterials with negative mass and modulus based on translational resonance. Int J Solids Struct. 2019;162:271–84.
[14] Imbalzano G, Linforth S, Ngo T, Lee PVS, Tran P. Blast resistance of auxetic and honeycomb sandwich panels: comparisons and parametric designs. Compos Struct. 2018;183:242–61.
[15] Qiao J, Chen C. Impact resistance of uniform and functionally graded auxetic double arrowhead honeycombs. Int J Impact Eng. 2015;83:47–58.
[16] Ma Q, Zhang YH. Mechanics of fractal-inspired horseshoe microstructures for applications in stretchable electronics. J Appl Mech. 2016;83(11):111008.
[17] Bettini P, Airoldi A, Sala G, Di Landro L, Ruzzene M, Spadoni A. Composite chiral structures for morphing airfoils: numerical analyses and development of a manufacturing process. Compos Part B Eng. 2010;41(2):133–47.
[18] Kuribayashi K, Tsuchiya K, You Z, Tomus D, Umemoto M, Ito T. Self-de-ployable origami stent grafts as a biomedical application of Ni-rich TiNi shape memory alloy foil. Mater Sci Eng A. 2006;419(1–2):131–7.
[19] Rogers JA, Someya T, Huang Y. Materials and mechanics for stretchable electronics. Science. 2010;327(5973):1603–7.
[20] Benouhiba A, Wurtz L, Rauch JY, Agnus J, Rabenorosoa K, Clevy C. Nanorobotic structures with embedded actuation *via* ion induced folding. Adv Mater. 2021;33(45):2103371.
[21] Liu H, Jin X, Zhou DK, Yang QH, Li LQ. Potential application of functional micro-nano structures in petroleum. Pet Explor Dev. 2018;45(4):745–53.
[22] Ko J, Bhullar S, Cho Y, Lee PC, Jun MBG. Design and fabrication of auxetic stretchable force sensor for hand rehabilitation. Smart Mater Struct. 2015;24(7):75027.
[23] Novak N, Vesenjak M, Ren Z. Auxeticcellular materials-a review. Stroj Vestn-J Mech Eng. 2016;62(9):485–93.
[24] Cosserat E, Cosserat F. Théorie des corps déformables. Vol. 81, Paris: A. Hermann; 1909. p. 67
[25] Eringen AC. Linear theory of micropolar elasticity. J Math Mech. 1966;15:909–23.
[26] Eringen AC. Microcontinuum field theories I: foundations and solids. New York, USA: Springer; 1999.
[27] Wu WW, Hua WX, Qian G, Liao HT, Xu X, Berto F. Mechanical design and multifunctional applications of chiral mechanical metamaterials: a review. Mater Des. 2019;180:107950.
[28] Liu XN, Huang GL, Hu GK. Chiral effect in plane isotropic micropolar elasticity and its application to chiral lattices. J Mech Phys Solids. 2012;60(11):1907–21.
[29] Frenzel T, Kadic M, Wegener M. Three-dimensional mechanical metamaterials with a twist. Science. 2017;358(6366):1072–4.
[30] Ma C, Lei H, Hua J, Bai Y, Liang J, Fang D. Experimental and simulation investigation of the reversible bi-directional twisting response of tetra-chiral cylindrical shells. Compos Struct. 2018;203:142–52.
[31] Wu W, Geng L, Niu Y, Qi D, Cui X, Fang D. Compression twist deformation of novel tetrachiral architected cylindrical tube inspired by towel gourd tendrils. Extrem Mech Lett. 2018;20:104–11.
[32] Zheng BB, Zhong RC, Chen X, Fu MH, Hu LL. A novel metamaterial with tension-torsion coupling effect. Mater Des. 2019;171:107700.
[33] Stachiv I, Alarcon E, Lamac M. Shape memory alloys and polymers for MEMS/NEMS applications: review on recent findings and challenges in design, preparation, and characterization. Metals. 2021;11(3):415.
[34] Stroud H, Hartl D. Shape memory alloy torsional actuators: a review of applications, experimental investigations, modeling, and design. Smart Mater Struct. 2020;29(11):113001.
[35] Atli K, Karaman I, Noebe RD, Bigelow G, Gaydosh D. Work production using the two-way shape memory effect in NiTi and a Ni-rich NiTiHf high-temperature shape memory alloy. Smart Mater Struct. 2015;24:125023.
[36] Grummon DS, Shaw JA, Foltz J. Fabrication of cellular shape memory alloy materials by reactive eutectic brazing using niobium. Mater Sci Eng A. 2006;438–440:1113–8.
[37] Machado G, Louche H, Alonso T, Favier D. Superelastic cellular NiTi tube-based materials: Fabrication, experiments and modeling. Mater Des. 2015;65:212–20.
[38] Hassan MR, Scarpa F, Ruzzene M, Mohammed NA. Smart shape memory alloy chiral honeycomb. Mater Sci Eng A. 2008;481–482:654–7.
[39] Kanik M, Orguc S, Varnavides G, Kim J, Benavides T, Gonzalez D, et al. Strain-programmable fiber-based artificial muscle. Science. 2019;365(6449):145–50.
[40] Maziz A, Concas A, Khaldi A, Stålhand J, Persson NK, Jager EWH. Knitting and weaving artificial muscles. Sci Adv. 2017;3(1):e1600327.
[41] Liu D, Tarakanova A, Hsu CC, Yu M, Zheng S, Yu L, et al. Spider dragline silk as torsional actuator driven by humidity. Sci Adv. 2019;5(3):eaau9183.
[42] Acome E, Mitchell SK, Morrissey TG, Emmett MB, Benjamin C, King M, et al. Hydraulically amplified self-healing electrostatic actuators with muscle-like performance. Science. 2018;359(6371):61–5.

[43] Kellaris N, Venkata VG, Smith GM, Mitchell SK, Keplinger C. Peano-HASEL actuators: muscle-mimetic, electrohydraulic transducers that linearly contract on activation. Sci Robot. 2018;3(14):eaar3276.
[44] Jiang S, Sun D, Zhang Y, Hu L. Deformation behavior and microstructure evolution of NiTiCu shape memory alloy subjected to plastic deformation at high temperatures. Metals. 2017;7(8):294.
[45] Tadayyon G, Guo Y, Mazinani M, Zebarjad SM, Tiernan P, Tofail SA, et al. Effect of different stages of deformation on the microstructure evolution of Ti-rich NiTi shape memory alloy. Mater Charact. 2017;125:51–66.